PCCP

Accepted Manuscript

ROYAL SOCIETY OF CHEMISTRY

www.rsc.org/pccp

Journal Name

ARTICLE

Heterogeneous Photo-Fenton Reaction on Hematite (α-Fe_2O_3) {104}, {113} and {001} Surface Facets

Received 00th January 20xx,
Accepted 00th January 20xx

DOI: 10.1039/x0xx00000x

www.rsc.org/

J. Y. T. Chan,[a, b] S. Y. Ang,[a, b] E. Y. Ye, [a] M. Sullivan[c], J. Zhang,[c, *] and M. Lin[a, *]

The exposed surface facets play an important role in determining the catalytic performance of nanostructured materials. In this study, we report the synthesis of hematite nanoparticles with three varying morphologies with exposure of well-controlled {104}, {113} and {001} surfaces. The better shape control of hematite particles has provided a direct correleation between the surface facets and the photocatalytic performance. The catalytic photodegradation of MB using hematite nanoparticles reveals that the reaction follows heterogeneous photo-Fenton process under visible light irradiation. The catalytic performance of hematite surface facets follows the order of {113} > {104} > {001}. Density Function Theory (DFT) calculation were conducted to demonstrate the atomic surface structures and corresponding charge distribution. The results indicate the catalytic activity depends on surface atom arrangements as well as the number and the type of surface terminated hydroxyl groups to underlying Fe atoms, where low valence states of Fe on {104} and {113} plane has highest probability to be oxidized by H_2O_2 and concurrent generated $Fe^{(3+x)+}$ sites are more electronegative to accept electrons from activated dye molecules. The findings are of fundamental importance to understand the surface-dependence of photocatalytic properties, thus shedding new light on the catalytic application of hematite particles.

Introduction

The physical and chemical properties of nanostructured catalysts are greatly affected by their size, morphology and composition. Since the heterogeneously catalytic reaction always occurs on the surface of crystals, the exposed surface facets play an important role in determining the catalytic performance. Therefore, nanostructured materials with controlled crystallographic orientation may exhibits unique reactivity, selectivity and stability due to their particular surface arrangement and active sites. For example, TiO_2 single crystals exposed with large percentage of {001} facets show a higher catalytic activity than {101} planes.[1] CeO_2 {100} surface is more active than {111} for adsorption of dissociated oxygen species.[2] The photodegradation rate of dye on {111} bounded AgBr is four times higher than that on {100} enclosed AgBr particles.[3] In addition, facet-controlled nanocrystals offer us an opportunity to study surface-structure dependent properties and deepen our understanding on structure-property relationship, thus establishing groundwork for rational design of catalysts with better performance.

Hematite (α-Fe_2O_3) is an environmentally friendly semiconductor material with wide applications as catalysts, adsorbents, batteries and pigments etc.[4–14] The commonest shapes for hematite crystals are rhombohedral, platy and rounded, where the {102, {104}, {001} and {113} planes dominate in most hematite crystals.[6] Recently, many efforts have been made to study the catalytic properties of hematite particles with defined morphologies and surface facets. Due to different absorption ability of CO and oxygen species on hematite facets, the catalytic activity to the oxidation of CO follows the order of {012} > {113} > {001}, while the organic gas sensing ability follows the order of {113} > {012} > {001}.[15] Li et al. reported that α-Fe_2O_3 nanorods with exposed {110} surface showed a higher activity for CO oxidation than the other facets owing to the higher density of Fe atoms on {110} plane.[16] The surface-dependent properties were also widely investigated by photo degradation of organic molecules on hematite surfaces.[17-22] The visible light induced rhodamine B degradation over hematite nanoparticles revealed an orders of {110} > {012} >> {001}.[17]

To date, systematic studies on the surface-structure dependent catalytic properties of hematite crystals with controlled shape and morphology are still lacking, partly due to the lack of α-Fe_2O_3 nanoparticles with various well-developed crystal facets in each published studies,[15-19] or owing to the incomplete analysis and characterization of the surface

[a] Institute of Materials Research and Engineering, A*STAR (Agency for Science, Technology and Research), 3 Research Link, S117602, Singapore. Email: m-lin@imre.a-star.edu.sg; Tel.: 65-6874 5374, Fax: 65-6874 4778.
[b] School of Applied Science, Temasek Polytechnic, 21 Tampines Avenue 1, S529757, Singapore.
[c] Institute of High Performance Computing, A*STAR (Agency for Science, Technology and Research), 1 Fusionopolis Way #16-16 Connexis S138632, Singapore. Email: zhangj@ihpc.a-star.edu.sg; Tel.: 65-6419 1340

† Footnotes relating to the title and/or authors should appear here. Electronic Supplementary Information (ESI) available: [details of any supplementary information available should be included here]. See DOI: 10.1039/x0xx00000x

crystallographic orientations in those efforts.[21-30] This has made direct correlation between surfaces and related catalytic properties difficult. Recently, we have reported the growth mechanism of rhombohedral and octadecahedral α-Fe_2O_3 nanoparticles in hydrothermal process and revealed the surface crystallographic orientations using high resolution TEM images and electron tomography.[31, 32] Therefore, facet-controlled synthesis of hematite nanoparticles and their surface dependent catalytic properties can be further investigated based our previous results.

In this study, we report the synthesis of hematite nanoparticles with three varying morphologies and well-controlled {104}, {113} and {001} surface facets. The catalytic performance on the degradation of Methylene Blue (MB) in aqueous solution under visible light irradiation has been studied. The better shape control of hematite particles has provided a direct and clear relationship between surface facets and photocatalytic performance. Density Function Theory (DFT) calculation were conducted to demonstrate the atomic surface structures and corresponding charge distribution. On the basis of experimental and simulation results, we propose that the photocatalytic property can be correlated to the oxidation states of Fe on hematite surface. The findings are of fundamental importance to understand the surface-dependence of photocatalytic properties.

Experimental

Synthesis

Three types of polyhedral α-Fe_2O_3 particles have been synthesised by the facile hydrothermal methods. (1) Rhombohedral α-Fe_2O_3 nanoparticles were prepared in ethanol solution. Typically, 2 mmol of ferric chloride hexahydrate ($FeCl_3 \cdot 6H_2O$) and 4 mL of ammonia hydroxide (14.0%) were dissolved in 30 mL of absolute ethanol. The mixture was stirred for 10 min at room temperature and then transferred into a 50 ml Teflon lined autoclave (Fisher Scientific). The autoclave was heated at 180 ^{o}C for 24 hrs. (2) Octadecahedral α-Fe_2O_3 nanoparticles with a hexagonal bipyramid shape were synthesized in an aqueous phase. 1 mmol of $FeCl_3 \cdot 6H_2O$, 0.12 mL of ammonia (14 %) and 1.6 mL of sodium fluoride (NaF) solution (0.2 M) were mixed in 30 mL of deionized (DI) water and treated in autoclaves at 180 ^{o}C for 24 hrs. (3) Hexagonal nanoplate α-Fe_2O_3 nanoparticles were fabricated in the mixture of de-ionized (DI) water and ethanol (1:30) solution. 2 mmol of $FeCl_3 \cdot 6H_2O$ and 2.0 g of sodium acetate were dissolved in 30 mL water-ethanol mixtures and hydrolysed in autoclaves at 180 ^{o}C for 12 hours. After hydrothermal reaction, the precipitate was collected by centrifuge and washed with ethanol and DI water respectively. The final α-Fe_2O_3 powders were obtained by drying in vacuum oven overnight and being calcined at 400 ^{o}C for 5 hours in air.

Characterization

The shape and structural analysis of the obtained α-Fe_2O_3 nanoparticles were performed on a JEOL-7600F Scanning Electron Microscope (SEM), an FEI Titan 80/300 Scanning/Transmission Electron Microscope (TEM) (200 kV) and an X-ray diffractometer with Cu $K\alpha_1$ radiation (Bruker GADDS, λ=1.5406 Å). The surface species and iron oxidation states were measured by the X-ray Photoelectron Spectroscopy (XPS) (ESCALAB 2201-XL, THERMO ELECTRON, VG Company). UV-Vis spectrometry was carried out with a Shimadzu UV-1800 UV-VIS spectrophotometer. The Brunauer-Emmett-Teller (BET) specific surface area was measured by a Micrometrics ASAP with a Physisorption Analyser.

Photo-Fenton catalytic Evaluation

The catalytic activity of α-Fe_2O_3 nanoparticles were evaluated by degradation of Methylene Blue (MB) in aqueous solution under illumination. 3 mg of α-Fe_2O_3 catalyst was dispersed with 7.5 mL of MB (50 mg/L) in a 20 mL vial. The suspension was magnetically stirred in darkness for 1 hour to reach an adsorption-desorption equilibrium, followed by addition of 7.5 mL of hydrogen peroxide solution (H_2O_2, 35%) in the mixture. The suspension was illuminated by a 500-W Philips Halolite lamp. No cut-off filter was used during the degradation reaction. However, the glass flask has an absorbance at UV light region (< 350 nm measured by UV-Vis spectrum), thus blocking some light to the solution. The light intensity was then measured around 35 mW/cm^2 after glass conical flask. Every 30 minutes, the illumination was blocked by a box and a 3 mL of aliquot was extracted, centrifuged and analysed by UV-Vis spectrometer. The aliquot was sonicated and re-mixed with stock solution. The concentration of MB was determined by measuring the maximum absorbance intensity at 664 nm. A linear relationship was obtained for concentration of MB and absorption of the solution (Figure S1 in supplementary information). The comparison samples were conducted parallel without light irradiation by covering the vial with 2 layers of aluminium foil.

Computational Details

DFT calculations were performed using the Vienna Ab Initio Simulation Package (VASP)[33, 34] in which a plane-wave basis set is used. The electron-ion interaction was modelled by the projector-augmented wave (PAW) method.[35, 36] The spin-polarized GGA (generalized-gradient approximation) scheme with the Perdew-Burke-Enzerhoff (PBE) form was used for the exchange and correlation functional.[37] The plane-wave cutoff energy was set to 400 eV. The rotationally invariant DFT+U method was applied to treat the on-site coulomb interaction of d electrons in Fe ions.[38] Here, the effective U-J value was set to 4.3 eV, which has been validated in literatures to study bulk and surfaces of hematite.[39-42]

α-Fe_2O_3 is antiferromagnetic with parallel magnetic moments within the Fe-Fe bilayer and antiparallel to the neighbouring bilayer.[43] We fully optimized the bulk structure, leading to the lattice constant of a = 5.03 Å and c = 13.72 Å, which are in good agreement of the experimental values of *a* = 5.0356 Å and *c* = 13.7489 Å (JCPDS No. 33-664).

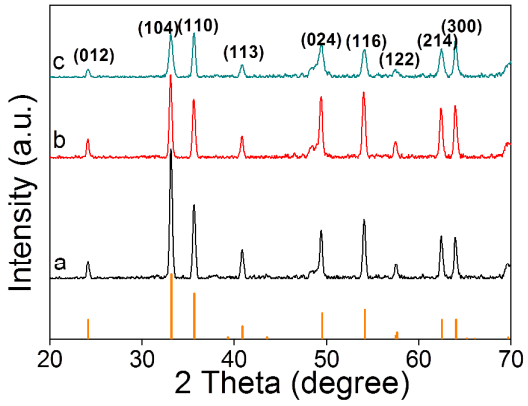

Fig. 1. XRD patterns of the nanoparticles with different shapes: (a) Rhombohedron; (b) Hexagonal Bipyramid; (c) Hexagonal Nanoplate. The bottom lines indicate the position of the standard peaks of hematite α-Fe_2O_3 with a rhombohedral structure (JCPDS 33-664).

Results

Figure 1 shows the XRD patterns of annealed α-Fe_2O_3 samples with three different morphologies. All the particles, synthesized with different methods, can be assigned to a rhombohedral phase (hematite α-Fe_2O_3, JCPDS No. 33-664) without the presence of any other crystalline impurities or intermediates. The strong and sharp diffraction peaks indicates a good crystallinity of the synthesised nanoparticles. (104) peak becomes weaker and broader from Figure 1a to Figure 1c while (110) peak maintaining its height, indicating morphology transforms from the better crystal development in the *c* direction to that in *a* direction.[4]

SEM images in Figure 2 display the typical morphology of α-Fe_2O_3 particles prepared by three hydrothermal synthesis routes. The preferential adsorption of anions on the surface could alter the surface energies and restrict crystal growth in certain directions, thereby promoting the growth of crystal into certain morphologies. In this paper, the synthesis of α-Fe_2O_3 nanoparticles with defined crystal facets was achieved by facile one-step hydrothermal/solvothermal reactions through fine-tuning of the solution medium or addition of foreign anions (fluorine or acetate).[31, 32, 44] In real hydrothermal/solvothermal reactions, the shape formation is finally realized by the dynamic process, such as oriented attachment and Oswald ripening processes (dissolution-reprecipitation).[31, 32, 45, 46]

Thus in ethanol medium, the forced hydrolysis of Fe^{3+} resulted in the formation of hematite particles with a rhombohedral shape, enclosed by six {104} planes, as shown in Figure 2a and our previous study.[31] The adjustment on the ratio between ethanol and water provided a delicate balance on the dissolution and precipitation of Fe^{3+} on crystals during solvothermal reaction, where the limited solubility and diffusion rate in ethanol reduced the etching of as-grown crystals and gave rise to the formation of particles with sharp surfaces and edges. In comparison to the shape of original α-Fe_2O_3 nanoparticles obtained immediately after hydrothermal reaction, the calcination at 400 ^{o}C for 5 hours resulted in the formation of rhombohedral α-Fe_2O_3 nanoparticles with slight rounding at corners. However, the major exposed surface is still {104} plane, with the total specific surface area measured at 6.8 m^2/g.

With addition of F^- in water, hematite α-Fe_2O_3 nanoparticles crystallized in a hexagonal bipyramid shape, which was an octadecahedron enclosed by twelve {113} side surfaces and six {104} top surfaces,[32] as shown in Figure 2b. The area of {104} surface occupies ~5% of total surface area. The specific surface area of hexagonal bipyramid particles after calcination is 4.6 m^2/g.

The adsorption of acetate anions on hematite surface led to the formation of α-Fe_2O_3 nanoparticles with a hexagonal plate shape. The synthesis procedure followed the method in literature elsewhere,[44] where the nanoplate particles have been reported to be enclosed by two large symmetric {001} planes and six {102} side surfaces. However, hematite has a rhombohedral crystal structure (space group $R\bar{3}C$), where {102} family planes only have 3-fold symmetry. To get insight into the shape and structure of nanoplate products, the obtained α-Fe_2O_3 nanoplates (Figure 2c) were further analyzed by diffraction patterns and high-resolution TEM (HRTEM) images. It should be noted that the lattice fringes observed in high resolution TEM images usually cannot be assigned to the surface facets except the exposed surfaces are parallel to the

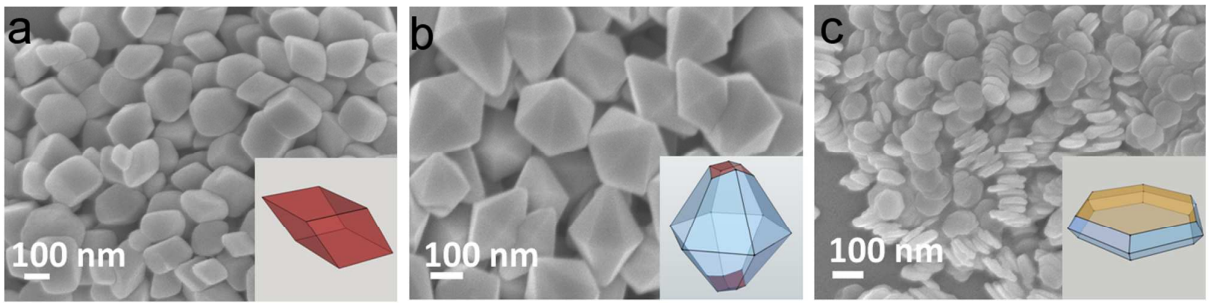

Fig. 2. SEM images of α-Fe2O3 nanoparticles after 400 °C calcination: (a) rhombohedron; (b) hexagonal Bipyramid; (c) hexagonal Nanoplate. Inset shows the schematic diagram of the corresponding particles. Red: {104}; blue: {113}; yellow: {001}.

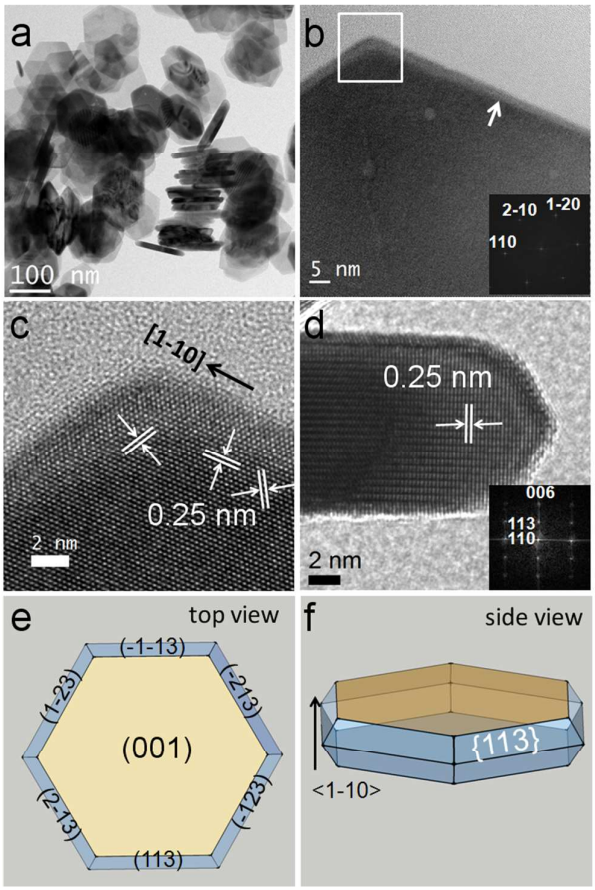

Fig. 3. Structural analysis of α-Fe_2O_3 hexagonal nanoplate particles: (a) Low magnification TEM image; (b, c) HRTEM image and corresponding FFT showing the top-view of the nanoplate; (d) side-view of the plate particles showing the {113} surfaces; (e, f) schematic diagram of nanoplate from top and side view.

electron beam.[31, 32]

Figure 3a shows a low magnification TEM image of α-Fe_2O_3 hexagonal nanoplate nanoparticles, with an average width of ~140 nm and thickness between 7 to 9 nm. The vertically aligned particles reveal wedge-shaped edges. When the α-Fe_2O_3 nanoplate is tilted along [*001*] zone axis (Figure 3b and 3c), it lies flat on TEM supporting membrane and intensity of six side edges appears lower than the center part due to a thinner edge (highlighted by the white arrow). A fast Fourier transformed (FFT) image from the high resolution image demonstrates a single crystalline structure of α-Fe_2O_3 nanoplate without the presence of twins or stacking faults. The lattice spacing measured in HRTEM image is 0.25 nm, corresponding to the distance between {110} planes. Therefore, $(\bar{1}20)$, $(\bar{2}10)$, (110) planes are parallel to the edge of plates, and the edges are along [*210*], [*120*] and [*1-10*] directions. Hence, the exposed edge facets are expected to be visualized along [*1-10*] direction in TEM. Figure 3d shows the side view of a nanoplate particle orientated along [*1-10*] direction, the exposed two basal plane could be indexed to (001), $(00\bar{1})$ planes and two side surfaces are (113) and $(1\bar{1}3)$ planes. The perfectly resolved lattice spacing of 0.25 nm

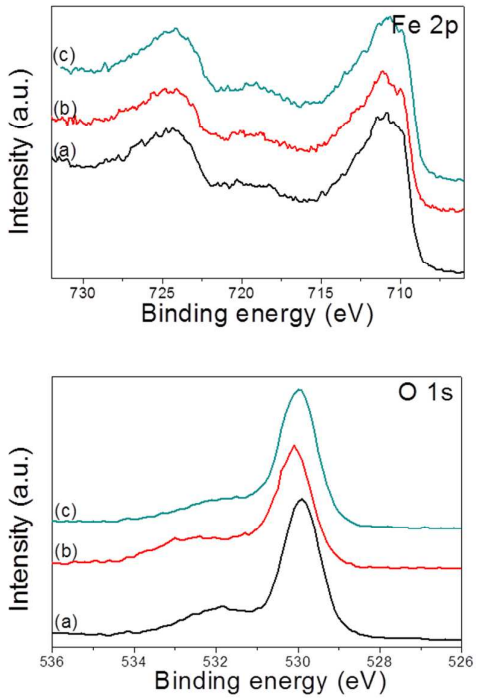

Fig. 4. Fe 2p and O 1s XPS spectra of α-Fe2O3 nanoparticles with (a) rhombohedral, (b) hexagonal bipyramid, and (c) hexagonal nanoplate shapes.

corresponds to the distance between hematite (110) planes, which is parallel to the edge of plates and in agreement with the plane-view analysis in Figure 3c. Therefore, the α-Fe_2O_3 hexagonal nanoplate is enclosed by two {001} basal planes and twelve {113} side planes, with {113} surface facets occupying ~5 % of total surface area based on a simple estimation from the average diameter and thickness of the nanoplates. Total surface area measured by BET is 15.4 m^2/g. The schematic drawings of α-Fe_2O_3 shapes and plane indices are shown in Figure 3e and 3f.

On the basis of above analysis and our published results, it is interesting to note that the dominantly exposed facets for hydrothermal synthesized α-Fe_2O_3 nanoparticles are {104}, {113} and {001} planes. The rhombohedral, hexagonal bipyramid and hexagonal nanoplate nanoparticles can be unambiguously assigned to a single crystal structure with dominantly exposed {104}, {113} and {001} planes respectively. The crystal development evolves from *c* direction to *a* direction, in good agreement with result from XRD analysis. The hydrothermal reaction conditions change the proportion between these planes, resulting in the formation of hematite α-Fe_2O_3 particles with distinctive shapes. The schematic diagrams of α-Fe_2O_3 particles are shown in inset in Figure 2 respectively.

The surface iron oxidation states and the surface species on various facets were revealed by XPS. As shown in Figure 4, no obvious difference has been observed from Fe 2p and O 1s peak on three α-Fe_2O_3 samples. The Fe 2p3/2 and 2p1/2 is located at 710.8 eV and 724.3 eV respectively, in agreement

with the reported values for Fe^{3+}.[15, 17, 18] The O 1s peak at 530.0 eV can be assigned to lattice O^{2-} binding to Fe. A weak peak located at 532 eV is attributed to adsorbed OH or chemisorbed oxygen.[15] Figure S4 in supplementary information demonstrates the F 1s peak for hexagonal bipyramid particles after different washing periods. It is clearly shown that almost all fluorine ions can be removed from the surface of hexagonal bipyramid α-Fe_2O_3 particles after three repeated washing procedures. The adsorbed water, which was indicated by the peak around 533 eV in O 1s spectra in Figure S5, can be removed by calcination process.[18] It is also shown that chlorine ions can be totally removed by washing process, as no chlorine being observed in XPS results (Figure S5). Therefore, the analyses from XPS suggest that clean surfaces are obtained after washing and calcination process for three faceted hematite particles.

A UV-Vis spectrometer was utilized to determine the absorbance peak of the nanoparticles, which was then used to calculate the band gap of hematite nanoparticles using Tauc relation. The Tauc relation was given as $(\alpha h\nu)^n = A_o (h\nu - E_g)$, whereby α is the absorption coefficient (cm^{-1}), hν is the photon energy (eV), E_g is the optical band gap (eV) and n is the optical transition value. A direct band gap will have an optical transition value of n = 2 while an indirect band gap will have an optical transition value of n = 0.5. The indirect band gaps of rhombohedral, hexagonal bipyramid, and hexagonal nanoplate α–Fe_2O_3 were 2.29 eV, 2.25 eV, and 2.20 eV respectively (Figure S7 in supplementary information). Studies have shown that hematite has an indirect (phonon-assisted) band gap transition of 1.9 eV to 2.3 eV,[4, 47] coinciding with the band gaps of our synthesized α–Fe_2O_3 nanoparticles. The slight difference in bandgap measurement could be caused by the morphological effects, where the light scattering and absorption coefficient are influenced by the shape of the particles and crystallographic orientation.[4] The characterization results for three kinds of α–Fe_2O_3 nanoparticles are listed in Table 1.

Faceted-controlled α–Fe_2O_3 nanocrystals are the optimum candidate to study surface-structure dependent properties and deepen our understanding on structure-property relationship. To evaluate the surface effect on catalytic property of α–Fe_2O_3 nanocrystals, the photo-assisted degradation of Methylene Blue (MB) was conducted as a model reaction in this study. Figure 5 shows the degradation efficiency of Methylene Blue (MB) under different reaction conditions over α–Fe_2O_3 nanocrystals with a rhombohedral shape. An enlarged figure was demonstrated in the supplementary information to provide a better view of some degradation conditions. The concentration of MB is linearly proportional to the absorption of the solution. Thus, we can obtain the concentration during the catalytic degradation processes by reading the absorption of each solution.

Table 1. Properties of α–Fe_2O_3 nanoparticles prepared by various routes.

	Structure	size (nm)	Surface Facets	Surface area (m^2/g)	Bandgap (eV)
Rhombohedron		256.1± 36.0	{104}	6.79± 0.06	2.29
Hexagonal Bipyramid	rhombohedral	365.2± 84.9	~5% {104} ~95% {113}	4.63± 0.02	2.25
Hexagonal Nanoplate		136.8± 17.8	~5% {113} ~95% {001}	15.45± 0.02	2.20

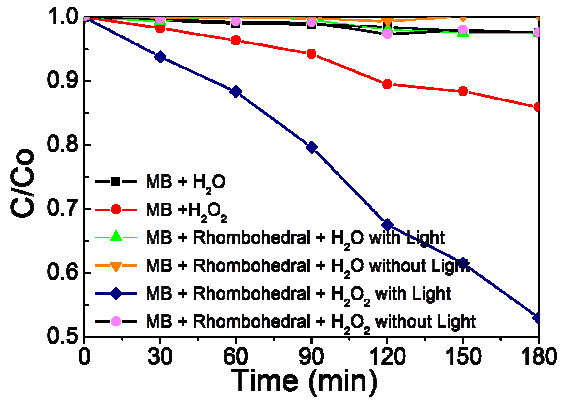

Fig. 5. Degradation of Methylene Blue (MB) (50mg/L) over rhombohedral α–Fe_2O_3 particles under different reaction conditions. C is the absorbance after visible-light irradiation and C_0 is the initial concentration.

The results suggest that the MB is stable in water under visible light irradiation. However, 15% MB can be decomposed after 180 min with the addition of H_2O_2 in the water, probably caused by the active hydroxyl radicals ($OH^{\bullet}$) released from the autogenously decomposition of H_2O_2. The degradation rate of MB will be accelerated after mixing the rhombohedral α–Fe_2O_3 catalysts with H_2O_2 solution. For comparison, the degradation of MB with hematite catalysts and H_2O_2 does not occur in the dark. This means that H_2O_2 and light are required for the degradation of MB on hematite catalysts, and this process could follow heterogeneous photo Fenton reaction[17] with a redox cycle between Fe^{2+} and Fe^{3+} on catalyst surface. The heterogeneous photo Fenton reaction is an advanced oxidation process that produces active $OH^{\bullet}$ radicals from Fe^{2+} and H_2O_2, which is proposed as follows:[17, 48, 49]

$$MB + h\nu \rightarrow MB^* \quad (1)$$

$$MB^* + Fe^{3+}/\text{hematite} \rightarrow dye^{+\bullet} + Fe^{2+}/\text{hematite} \quad (2)$$

$$Fe^{2+}/\text{hematite} + H_2O_2 \rightarrow OH^{\bullet} + Fe^{3+}/\text{hematite} + OH^- \quad (3)$$

$$MB + OH^{\bullet} \rightarrow \text{degradation products} \quad (4)$$

The generation of Fe^{2+} on hematite crystal is the key step for the production of active $OH^{\bullet}$ radicals in this experiment. The comparison experiments, as shown in Figure 5 and Figure S9, suggested that the other possible reaction pathways for $OH^{\bullet}$ radical generation can be excluded in this photodegradation process. Firstly, the generation of $OH^{\bullet}$ radicals from direct light excitation of α–Fe_2O_3 catalysts can be

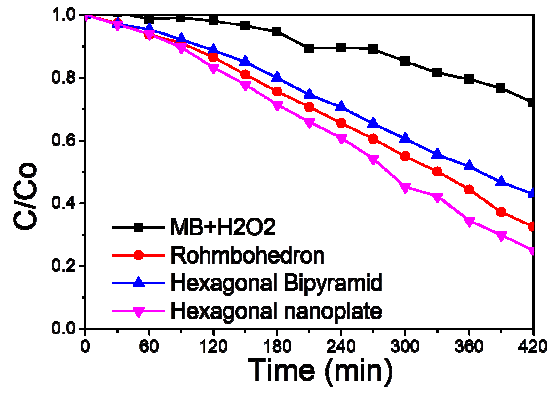

Figure 6. Photo-catalytic degradation of Methylene Blue (MB) over α–Fe_2O_3 particles with different facets in the presence of H_2O_2

ignored. Hematite is a semiconductor material with a bandgap of 2.2 eV. The electron-hole pairs can be formed upon excitation from visible light irradiation. Theoretically, the photo generated holes could accept an electron from water and yield $OH^{\bullet}$ radicals. However, this process does not occur in our photodegradation reaction. As shown in Figure 5, negligible degradation of MB is observed with simple illumination of hematite catalyst and water, mainly due to very low hole mobilities (10^{-2} $cm^2V^{-1}S^{-1}$) and very high electron-hole recombination rates (on the order of 10 ps) in hematite.[4, 50-52] The accumulation of photogenerated holes near the surface and high charge recombination rate lead to a poor water oxidation efficiency for Fe_2O_3 catalysts. Hence, the following reaction pathway to produce hydroxyl radicals is inefficient and could be excluded in the degradation of MB with α–Fe_2O_3 nanoparticles:

$$Fe_2O_3 + h\nu \rightarrow Fe_2O_3(e^- + h^+) \quad (5)$$

$$h^+ + H_2O \rightarrow HO^{\bullet} + H^+ \quad (6)$$

Secondly, since the degradation reaction was conducted in a neutral solution, the low solubility of hematite ($k \approx 3\times10^{-42}$ in low ionic solution at 25 °C)[4] leads to a low dissolution of iron from the hematite particles and produces limited dissolved aqueous Fe^{2+}/Fe^{3+} ions in solution. Thus, classical homogeneous Fenton reaction, usually conducted with Fe^{2+} / Fe^{3+} aqueous ions and in a narrow pH range of 2~4, is excluded in this reaction. This suggests that the dye degradation and Fe^{2+} / Fe^{3+} conversion with H_2O_2 mainly occur on the surface of hematite crystals rather than in solution.

It has been proposed that the Fe^{2+} can also be produced by the reduction of Fe^{3+} on catalyst surface with H_2O_2.[49] However, no degradation of dye was observed with assistance of H_2O_2 in dark without light irradiation. Thus, the following route for generation of Fe^{2+} is negligible in the reaction.[49]

$$Fe^{3+}/Fe_2O_3 + H_2O_2 \rightarrow Fe^{2+}/Fe_2O_3 + HO_2^{\bullet} + H^+ (7)$$

Therefore, the heterogeneous Photo-Fenton reaction is the major path for the MB degradation. Figure 6 presents typical degradation of MB concentration on α–Fe_2O_3 nanoparticles with different surface facets. It was found that the degradation rate was dependent on the room temperature, distance from the lamp, and the concentration of catalysts etc. In principle, the amount of catalyst will not affect the catalytic rate. However, the concentration of catalyst and MB determined the transmission of the light through the solution, the higher concentration, the lower light transmission. The light absorption by MB molecules significantly affected the activation of the MB. The low concentration of catalyst and low concentration of MB solution showed a higher catalytic degradation rate. Therefore, the same reaction conditions were applied during reaction and the results were averaged from different batches of experiments, which were listed in Table 2. The degradation rate and standard deviation for different catalysts are normalized by specific surface areas. Hexagonal bipyramid α–Fe_2O_3 nanoparticles with major exposed {113} facets exhibit the highest activity to the photo degradation to the MB, followed by rhombohedral {104} surfaces, and hexagonal nanoplate {001} planes. The order of plane activity was repeated with another two degradation conditions (Fig S10 and S11 in the supplementary information). This result is also in agreement with literature results({110} > {012} >> {001}),[17] if we correct some wrongly assigned crystallographic surfaces ({113}>{104}[22], {104}>{001})[23] in other literatures.

According to the surface and structural analysis by XPS, all of the surfaces are clean without any adsorption of foreign anions after proper washing procedures and calcine treatment. In addition, the differences in bandgap are also trivial, which is not enough to interpret the observed changes in the catalytic efficiency of MB on different faceted α–Fe_2O_3 nanoparticles. To provide insight into the origin of the surface catalytic activity, which critically depends on the surface topography, atom arrangements as well as the density and oxidation states of Fe atoms, DFT calculations were performed to simulate the α-Fe_2O_3 bulk and surfaces.

Table 2. Photo degradation rate and normalized rate constants of α–Fe_2O_3 particles with standard deviations.

	K (10^{-3} min^{-1})	Normalized K (10^{-4} /m^2·min)
Rhombohedron {104}	2.2±1.5	3.2±2.2
Bipyramid {113}	1.7±1.2	3.7±2.6
Plate {001}	0.8±0.7	1.7±2.6

Discussion

Hematite bulk has a rhombohedral structure with hexagonal closed-packed arrays of O^{2-} along the [*001*] direction.[47] One Fe

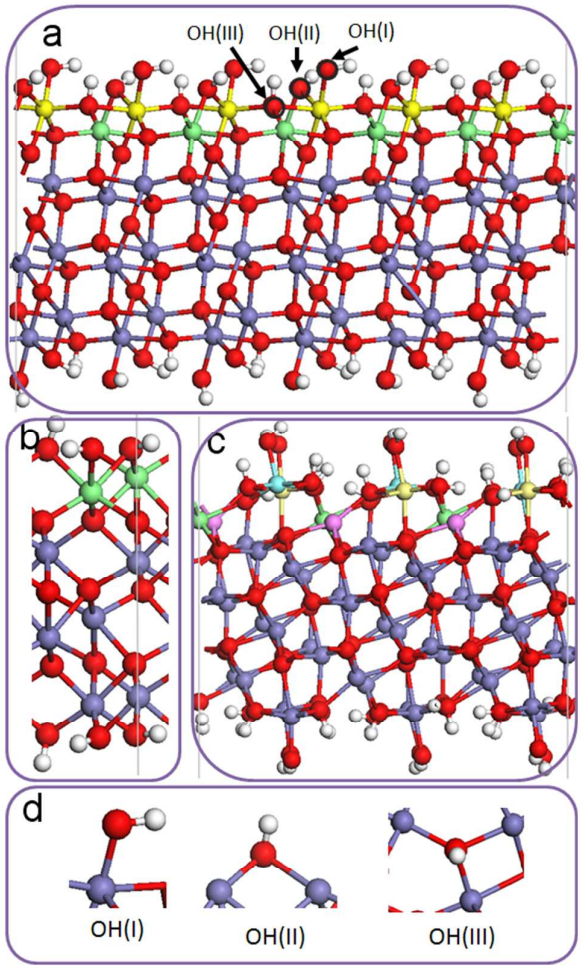

Figure 7. Side views of optimized α-Fe_2O_3 surfaces: (a) (104), where top-layer Fe atoms are in two groups highlighted by yellow and green colour; (b) (001), where top-layer Fe atoms are in green; and (c) (113), where top-layer Fe atoms are in four groups highlighted by yellow, blue, pink and green, respectively. (d) Schematic drawing of singly, doubly and triply terminating OH groups. Here, O is in red, H is in white and other colours represent Fe atoms.

atom bonds to six O, and each O atom is shared by four Fe, so the stoichiometry of hematite is Fe_2O_3 and each Fe-O bond has a charge of +1/2 theoretically.[4] We calculated bader charges[53] for Fe and O in hematite bulk and found that ionic charges are +1.76 for Fe and -1.18 for O, which are consistent with the values of +1.8 (Fe) and -1.2 (O) reported by Liao and co-workers.[42] The scale factor of bader charge to stoichiometric charge (Fe: +3 and O: -2) is 0.59. Based on the bulk structure, we further built α-Fe_2O_3(001), (104) and (113) surfaces to study atom arrangement and ionic charges.

α-Fe_2O_3 (001), (104) and (113) surfaces were simulated by a slab supercell approach with periodic boundaries. Exposure of calcined hematite particles to aqueous solution leads to the formation of surface hydroxyl groups.[54, 55] The very recent theoretical work indicated that hydroxylated Fe_2O_3 (001) surface is more stable than the corresponding O-terminated slab.[42] Thus, fully hydroxylated Fe_2O_3 surface models were considered in this work, where we built symmetric O-terminated Fe_2O_3 slab first, and then the H surface adsorption leads to terminating hydroxyl group. As shown in Figure 7, the O-terminated (001) surface is made up of four Fe bilayers and five O layers, (104) surface slab contains four Fe-O double layers, and the stepped (113) surface has four layers of Fe and O atoms. The thickness of considered slabs is ~ 9.2 Å for the (001) surface, 12.4 Å for the (104) surface, and 13.2 Å for the (113) surface, respectively. All atoms were allowed to be relaxed and a vacuum region of 12 Å was used, which is large enough to avoid interactions with imaging slabs.

Examination of surface hydroxyls reveals three types of terminating OH groups, bonding to one, two or three underlying Fe atoms.[4] For the ease of reference, we denoted these singly, doubly and triply coordinated OH groups as OH(I), OH(II) and OH(III), as shown in Figure 7d. Assuming a charge of -1 is assigned to OH group and O has a higher electronegative than Fe, each Fe-O bond carries theoretically a charge of +1, +1/2 and +1/3 for OH(I), OH(II) and OH(III) respectively. Our simulation results agree well with this hypothesis. As shown in Figure 7a, circled O atoms gain 0.97*e* (OH(I)), 0.50*e* (OH(II)) and 0.31*e* (OH(III)) from each bonding Fe atom (after modifications by the scale factor of 0.59). Thus, the Fe coordinated to OH(I)/OH(III) probably has a higher/lower oxidation state compared to the normal one in hematite bulk crystal. We noticed that surface Fe atoms are coordinated to different types and numbers of OH groups depending on the exposed crystal faces. Thus, the variation in the surrounding environment is most likely to affect electron-accepting/donating capacity of Fe atoms in the redox cycle.

In Figure 7b, both of the two surface Fe atoms on hematite (001) surface are coordinated to three OH(II), thus it shows bulk-like electronic structure, and the bader charge is +1.76 for which are less positive than the value on surface (001). The stepped α-Fe_2O_3 (113) surface is more complex. In Figure

Table 3. Bader charges (Fe), surface Fe density and surface hydroxyl density on various α-Fe_2O_3 surfaces.

α-Fe_2O_3	Bader Charge	corrected charge	Hydroxyl density (per nm^2) OH(I):OH(II) : OH(III)	Surface Fe density (per nm^2)
bulk	+1.76	+3		
(001)	+1.76	+3	0 : 13.7 : 0	9.1
(104)	+1.54, +1.72	+2.61,+2.92	5.4 : 5.4 : 5.4	10.7
(113)	+1.47,+1.42 +1.69,+1.77	+2.49,+2.41 +2.86, +3	4.4: 4.4 : 8.8	8.8

*Bader charge is value of surface Fe cations with the same bonding environment (as indicated in Figure 7). corrected charge = bader charge/0.59 (0.59 is the scale factor, which is obtained by a ratio between simulated bader charge in Fe_2O_3 bulk and stoichiometric charge in real (Fe: +3 and O: -2).

7c, there are four different types of Fe cations on the terrace and Fe, -1.21 for O in OH groups and +0.63 for H. However, on (104) surface, surface Fe atoms are terminated by OH(I), OH(II) and OH(III) with the ratio of 1:1:1(the density is 5.4: 5.4: 5.4/nm^2). As shown in Figure 7a, Fe cations in yellow and those in green have a bader charge of +1.54 and +1.72 respectively, step edge, which are coordinated to different numbers of OH(I), OH(II) and OH (III). Here, the relative density of OH(I), OH(II) and OH(III) is 4.4 : 4.4 : 8.8 per nm^2. There are more OH(III) on surface (113) than those on surface (104) (5.4/nm^2). According to DFT calculations, the four types of Fe cations on surface (113) (yellow, blue, pink. green in Figure 7c) lose 1.47*e*, 1.69*e*, 1.42*e*, and 1.77*e*, respectively. It should be noted that this delicate difference on oxidation states of surface Fe cannot be observed by XPS, which usually gives the accumulated electronic information from Fe atoms located from the surface to 5 nm deep subsurface.

Since the atomic density of Fe on three facets is similar to each other (Table 2), the difference in heterogenetic catalytic Fenton reaction may be caused by the surface charge statues. The density of Fe ions with 3+ valence state on (001) surface is higher than that on the other two planes, while the photocatalytic activity is lower than that of (113) and (104) facet. This suggests Fe ions with lower oxidation states on the surface may be more active than Fe^{3+}. In classical Fenton reaction, the charge transfer from Fe^{2+} to H_2O_2 occurs faster than the reduction of Fe^{3+} to Fe^{2+}.[49] Our simulation results indicate that the increasing order of the oxidation state for surface Fe follows (113) < (104) < (001), where Fe cations on (113) and (104) showing an oxidation state between 2+ and 3+. Hence, it implies that electron-rich Fe cations on surface (113) and (104) can easily initiate an electron transfer to H_2O_2 for the generation of OH radicals. The concurrently generated $Fe^{(3+x)+}$ (0<x<1) ions is more positive than the normal (Fe^{3+}). The more positive the charge is, the more likely the cation is reduced. That means the oxidized $Fe^{(3+x)+}$ ions are relatively easier to accept electron donation from photo activated MB molecules to produce the key $Fe^{(2+x)+}$ ions. Thus, compared to surface (001), surface (104) and (113) facilitate the Fe^{2+}/Fe^{3+} redox cycle, which leads to the higher catalytic activity for photo Fenton degradation of MB with H_2O_2.

Our calculations put into perspective a recent elegant experiment on spontaneous oxygen evolution reaction, which demonstrated that {001} face is the most electropositive and the {113} is the most electronegative.[56, 57] We suggest an easy electron transfer from more electronegative {113} facets to H_2O_2 resulting in the high catalytic performance in the photo Fenton reaction.

Conclusions

In conclusion, three faceted α–Fe_2O_3 nanoparticles enclosed by different crystal planes have been successfully synthesised by hydrothermal reactions. The rhombohedral, hexagonal bipyramid and hexagonal nanoplate nanoparticles can be unambiguously assigned to a single crystal structure with major exposed {104}, {113} and {001} planes respectively. The catalytic photodegradation of MB using hematite nanoparticles reveals that the reaction follows heterogeneous photo Fenton process under visible light irradiation. The catalytic performance of hematite surface facets follows the order of {113} > {104} > {001}. The results clearly indicate the catalytic activity strongly depends on surface atom arrangements as well as the number and the type of surface terminated hydroxyl groups to underlying Fe atoms, where {113} plane has highest probability to be oxidized by H_2O_2 and concurrent generated $Fe^{(3+x)+}$ site is more electronegative to accept electrons from activated dye molecules. Triply coordinated Fe atoms could be the most active sites for photo Fenton reactions.

In the present study, we intended to improve our understanding on the relationship between surface structures and catalytic properties. However, only ideal surfaces are considered without evaluating the influence of the surface reconstruction, defects, impurities and adsorption of OH^- and H^+. Future work is required on the more delicate characterization of surfaces and simulation of more realistic surfaces under different reaction conditions.

Acknowledgements

The financial support of IMRE (IMRE/12-1P0907, IMRE/13-1C0435) is gratefully acknowledged.

Notes and references

1 H. G. Yang, C. H. Sun, S. Z. Qiao, J. Zou, G. Liu, S. C. Smith, M. Q. Cheng, G. Q. Lu, *Nature* 2008, **453,** 638.
2 X. Wang, Z. Jiang, B. Zheng, Z. Xie, L. Zheng, *CrystEngComm* 2012, **14,** 7579.
3 H. Wang, J. Yang, X. Li, H. Zhang, J. Li, L. Guo, *Small* 2012, **8,** 2802.
4 R. M. Cornell, U. Schwertmann, the Iron Oxides: Structure, Properties, Reactions, Occurrences and Uses; Wiley-VCH Verlag, Weinhein, 2003.
5 M. A. Blesa, E. M. Matijevic, *Adv. Colloid Interface Sci.* 1989, **29,** 173.
6 U. Schwertmann, J. Friedl, H. Stanjek, *J. Colloid Interface Sci.* 1999, **209,** 215.
7 L. Wan, S. Yan, X. Wang, Z. Li, Z. Zou *CrystEngComm* 2011, **12,** 2727.
8 Z. Zhong, M. Lin, V. Ng, G. H. B. Ng, Y. Foo, A. Gedanken, *Chem. Mater.* 2006, **18**, 6031.
9 Z. Zhong, J. Highfield, M. Lin, J. Teo, Y. Han, *Langmuir* 2008, **24**, 8576.
10 H. Cao, G. Wang, L. Zhang, Y. Liang, S. Zhang, X. Zhang, *ChemPhysChem* 2006, **7**, 1897.
11 J. Yin, Z. Yu, F. Gao, J. Wang, H. Pan, Q. Lu, *Angew. Chem. Int. Ed.* **2010**, *49*, 6328.
12 X. Mou, X. Wei, Y. Li, W. Shen, *CrystEngComm* 2012, **14**, 5107.
13 M. Zhu, Y. Wang, D. Meng, X. Qin, G. Diao, *J. Phys. Chem. C* 2012, **116,** 16276.
14 J. Ma, T. Wang, X. Duan, J. Lian, Z. Liu, W. Zheng, *Nanoscale* 2011, **3**, 4372.
15 J. Ouyang, J. Pei, Q. Kuang, Z. Xie, L. Zheng, *ACS Appl. Mater. Interfaces* 2014, **13**, 12505.
16 X. Liu, J. Liu, Z. Chang, X. Sun, Y. Li, *Catal. Commun.* 2011, **12**, 530.

17 X. Zhou, J. Lan, G. Liu, K. Deng, Y. Yang, G. Nie, J. Yu, L. Zhi, *Angew. Chem. Int. Ed.* 2012, **51**, 178.
18 X. Zhou, H. Yang, C. Wang, X. Mao, Y. Wang, Y. Yang, G. Liu, *J. Phys. Chem. C* 2010, **114**, 17051.
19 J. Wu, J. Wang, H. Li, Y. Du, K. Huang, B. Liu, *J. Mater. Chem. A* 2013**, 1**, 9837.
20 J. Qu, Y. Yu, C. Y. Cao, W. G. Song, *Chem. Eur. J.* 2013, **19**, 11172.
21 S. Yang, Y. Xu, Y. Sun, G. Zhang, D. Gao, *CrystEngComm* 2012, **14**, 7915.
22 Y. Zhao, F. Pan, H. Li, T. Niu, G. Xu, W. Chen, *J. Mater. Chem.* A 2013, **1**, 7242.
23 S. Li, G. Qin, X. Meng, Y. Ren, L. Zuo, *J. Mater. Sci*. 2013, **48**, 5744.
24 X. Wang, J. Wang, Z. Cui, S. Wang, M. Cao, *RSC Adv.* 2014, **4**, 34387.
25 Z. Liu, B. Lv, D. Wu, Y. Sun, Y. Xu, *Particuology* 2013, **11**, 327-333.
26 Z. Liu, B. Lv, D. Wu, Y. Sun, Y. Xu, *Eur. J. Inorg. Chem.* 2012, 4076.
27 J. Yin, Z. Yu, F. Gao, J. Wang, H. Pang, Q. Lu, *Angew. Chem. Int. Ed.* 2010, **49**, 6328.
28 B. Lv, Z. Liu, H. Tian, Y. Xu, D. Wu, Y. Sun, *Adv. Funct. Mater.* 2010, **20**, 3987.
29 B. Xu, B. Huang, H. Cheng, Z. Wang, X. Qin, X. Zhang, Y. Dai, *Chem. Commun.* **2012**, *48*, 6529.
30 T. Van, H. G. Cha, C. K. Nguyen, S. Kim, M. Jung, Y. S. Kang, *Cryst. Growth Des.* **2012**, *12*, 862.
31 M. Lin, H. R. Tan, J. P. Y. Tan, S. Bai, *J. Phys. Chem. C* 2013, **117**, 11242.
32 M. Lin, L. Tng, T. Lim, M. Choo, J. Zhang, H. R. Tan, S. Q. Bai, *J. Phys. Chem. C* 2014, **118**, 10903.
33 G. Kresse, J. Hafner, *Phys. Rev. B* 1993**, 48**, 13115.
34 G. Kresse, J. Hafner, *Phys. Rev. B* 1994**, 49**, 14251.
35 P. E. Bloechl, *Phys. Rev. B* 1994**, 50**, 17953.
36 G. Kresse, D. Joubert, *Phys. Rev. B* 1999**, 59**, 1758.
37 J. P. Perdew, K. Burke, M. Ernzerhof, *Phys. Rev. Lett.* 1996, **77**, 3865.
38 S. L. Dudarev, G. A. Botton, S. Y. Savrasov, C. J. Humphreys, A. P. Sutton, *Phys. Rev. B* 1998, **57**, 1505.
39 N. J. Mosey, P. Liao, E. A. Carter, *J. Chem. Phys.* 2008, **129**, 014103.
40 P. Liao, E. A. Carter, *Phys. Chem. Chem. Phys.* 2011, **13,** 15189.
41 P. Liao, E. A. Carter, *J. Mater. Chem.* 2010, **20**, 6703.
42 P. Liao, J. A. Keith, E. A. Carter, *J. Am. Chem. Soc.* 2012, **134**, 13296.
43 A. Kiejna, T. Pabisiak, *J. Phys.: Condens. Matter* 2012, **24**, 095003.
44 L. Chen, X. Yang, J. Chen, J. Liu, H. Wu, H. Zhang, C. Liang, M. Wu, *Inorg. Chem.* 2010, **49**, 8411-8420.
45 J. P. Y. Tan, H. R. Tan, C. Boothroyd, Y. L. Foo, C. B. He, M. Lin, *J. Phys. Chem. C* 2011, **115**, 3544.
46 M. Lin, Z. Y. Fu, H. R. Tan, J. P. Y. Tan, S. C. Ng, E. Teo, *Cryst. Growth Des.* 2012, **12**, 3296.
47 K. Sivula, R. Zboril, F. L. Formal, R. Robert, A. Weidenkaff, J. Tucek, J. Frydrych, M. Gratzel, *J. Am. Chem. Soc.* 2010, **132**, 7436.
48 S. G. Kumar, L. G. Devi, *J. Phys. Chem. A* 2011, **115**, 13211.
49 E. Neyens, J. Baeyens, *J. Hazardous Mater.*2003, **98**, 33.
50 J. H. Kennedy, K. W. Frese, *J. Electrochem. Soc.* 1978, **125**, 709.
51 J. K. Leland, A. J. Bard, *J. Phys. Chem.* 1987, **91***,* 5076.
52 K. Sivula, F. Le Formal, M. Grätzel, *ChemSusChem* 2011, **4**, 432.
53 L. W. Finger, R. M. J. Hazen, *Appl. Phys.* 1980, **51**, 5361.
54 P. Liu, T. Kendelewicz, G. E. Jr. Brown, E. J. Nelson, S. A. Chambers, *Surf. Sci.* 1998, **417**, 53.
55 S. Yamamoto, T. Kendelewicz, J. T. Newberg, G. Ketteler, D. E. Starr, E. R. Mysak, K. J. Andersson, H. Ogasawara, H. Bluhm, M. Slameron, G. E. Jr. Brown, A. Nilsson, *J. Phys. Chem. C* 2010, **114**, 2256.
56 S. Chatman, P. Zarzycki, K. M. Rosso; *ACS Appl. Mater. Interface* 2015, **7**, 1550.
57 S. Chatman, P. Zarzycki, K. M. Rosso, *Phys. Chem. Chem. Phys.* 2013, **15**, 13911.